An Off-Lattice Hybrid Discrete-Continuum Model of Tumor Growth and Invasion

Junhwan Jeon,[†‡*] Vito Quaranta,[‡§] and Peter T. Cummings[†‡¶]
[†]Department of Chemical and Biomolecular Engineering, Vanderbilt University, Nashville, Tennessee; [‡]Vanderbilt Integrative Cancer Biology Center, Nashville, Tennessee; [§]Department of Cancer Biology, Vanderbilt University Medical Center, Nashville, Tennessee; and [¶]Nanomaterials Theory Institute, Center for Nanophase Materials Sciences, Oak Ridge National Laboratory, Oak Ridge, Tennessee

ABSTRACT We have developed an off-lattice hybrid discrete-continuum (OLHDC) model of tumor growth and invasion. The continuum part of the OLHDC model describes microenvironmental components such as matrix-degrading enzymes, nutrients or oxygen, and extracellular matrix (ECM) concentrations, whereas the discrete portion represents individual cell behavior such as cell cycle, cell-cell, and cell-ECM interactions and cell motility by the often-used persistent random walk, which can be depicted by the Langevin equation. Using this framework of the OLHDC model, we develop a phenomenologically realistic and bio/physically relevant model that encompasses the experimentally observed superdiffusive behavior (at short times) of mammalian cells. When systemic simulations based on the OLHDC model are performed, tumor growth and its morphology are found to be strongly affected by cell-cell adhesion and haptotaxis. There is a combination of the strength of cell-cell adhesion and haptotaxis in which fingerlike shapes, characteristic of invasive tumor, are observed.

INTRODUCTION

A tumor is characterized by abnormal growth of cells resulting from altered gene expressions or mutations. While the tumor grows and evolves, the mutations continue and the behavior of tumor cells departs from that of normal cells of the tissue. This solid neoplasm may destroy surrounding extracellular matrix (ECM), invade and penetrate into ECM by means of matrix-degrading enzymes (MDE), and thereby spread to other locations in the body by the process of metastasis (1).

The dynamics of tumor growth constitutes a complex process involving cell-cell and cell-ECM interactions, proliferation of individual cells, secretion of MDE, transport of nutrient, and so on, taking place at different scales both in space and in time (2). Although experimentally, it is difficult to isolate individual effects from a synchronously integrated tumor growth process while keeping other effects intact, mathematical modeling enables us to examine individual effects, one by one or in any combination, with relative ease. Thus, better understanding of tumor growth and invasion would be realized with the aid of mathematical models, which could ultimately improve therapeutic efficiency by predicting the outcome of a specific treatment on certain types of tumors. Hence, not surprisingly, there have been many attempts (3–16) to mathematically and computationally describe the dynamics of tumor growth.

In mathematical models, tumor cells are treated either as a continuous density distribution (3–6) or as discrete objects (7–16). Both approaches have their advantages as well as drawbacks, depending upon the phenomenon under consideration, and on the time- and space scale in which the phenomenon is studied. A continuum model deals with phenomena on larger spatial and temporal scales, and it is the easier model to analyze both analytically and computationally; however, it often fails to capture details of cell-level behavior. In a discrete model, it is relatively easy to describe the detailed behavior of individual cells, which includes random and biased cell migration (kinesis and taxis), cell-cell and cell-ECM interactions, and cell proliferation. On the other hand, the computational cost of a discrete model increases nonlinearly with system size, often limiting the size of the tumor that can be modeled. In general, the advantages in continuum models are drawbacks in discrete models and vice versa. Several hybrid continuum-discrete methods (8,9,11–15) for tumor growth have been developed to maximize advantages and minimize drawbacks by using both continuous and discrete levels, thus providing a more comprehensive understanding of cell migration leading to more accurate and efficient prediction of tumor morphology and potential for invasion.

Recently, the works of Anderson et al. (8,9) have attracted considerable attention due to the successful application of their hybrid discrete-continuum method to tumor growth and invasion, with the result of tumor morphology variation that depends upon tumor microenvironment conditions: Harsh tumor micro-environment conditions (e.g., hypoxia, heterogeneous ECM) lead to fingerlike tumor morphology with aggressive cells on the fingering margins, whereas mild microenvironment conditions (e.g., normoxia, homogeneous ECM) allow coexistence of aggressive with less-aggressive phenotypes that have smooth, noninvasive margins (9). Therefore, their simulation results suggest that differentiating therapy aimed at cancer-micro-environment interactions might be more useful than making the microenvironment harsher (e.g., by chemotherapy or antiangiogenic therapy).

Submitted February 20, 2009, and accepted for publication October 1, 2009.

*Correspondence: junhwan.jeon@vanderbilt.edu

Editor: Jason M. Haugh.

© 2010 by the Biophysical Society

0006-3495/10/01/0037/11 $2.00

doi: 10.1016/j.bpj.2009.10.002

However, the model of Anderson et al. has several drawbacks resulting from the use of a simple rule-based cellular automata model on square lattice, one of which is that, due to the limited set of possible directions and discrete displacement for cell movement with a certain probability, it does not adequately describe cell motility. Because cell migration is thought to be central to tumor growth and invasion, it is imperative to develop a more phenomenologically realistic and bio/physically relevant model that correctly describes cell motility by incorporating the experimentally observed superdiffusive behavior of mammalian cells. The model of Anderson et al. assumes diffusive cell motion on all timescales, whereas, experimentally, the mean-square displacement of mammalian epithelial cells typically showed superdiffusive motion on timescales of ~100 min (17). This behavior is easily reproduced in our off-lattice model, described in Model and Simulation. Apart from cell migration, in the Anderson model, other cellular phenomena such as cell-cell adhesion and cell-ECM interaction (haptotaxis) are described via heuristic stochastic terms resulting in the loss of physical and mechanical foundations of cell behavior.

Using an off-lattice model of cell motility with detailed forces describing cell-cell and cell-ECM interactions can provide us with a way to overcome the drawbacks of using a lattice model with heuristic stochastic terms for cell behavior, as 1), anisotropy effects on cell migration and tumor morphology can be reduced; and 2), physical and mechanical aspects of cell behavior can be more appropriately addressed. In particular, realistic modeling of cell motility, cell-cell adhesion, and cell-ECM interactions is needed as we seek to develop more realistic future models that include coarse-grained, molecular-based models for ECM.

The movement of individual cells is generally represented by a persistent random walk (PRW): For short observation times, the cells undergo persistent or ballistic motion, whereas for long observation times, the motion of the cells follows diffusive or random motion. To describe a PRW, the Langevin equation has been widely used not only in the fields of biology and ecology but also in statistical physics (18). One aim of this article is to develop a hybrid model of tumor growth and invasion with more-realistic description of cell migration using the Langevin equation. We also propose that it is valid to extend the PRW approach from single cell migration to large cell populations of cells growing as tumors. Due to difficulty in obtaining parameter values from idealized experiments, at this time we are using certain levels of biological abstraction that are presented in Table S1. These assumptions provide guidance for producing experimental data consistent with the hybrid model.

The other aim of this article is to study the effect of cell-cell adhesion and haptotaxis on tumor growth and its morphological behavior by performing systematic simulations of the off-lattice hybrid discrete-continuum (OLHDC) model. Tumor morphology analysis in our simulation will allow us to study the type of tumor associated with its geometry and dynamics, and to predict its malignant nature because the morphological asymmetry of tumors has been used as one of the experimental indicators of malignancy (19,20). Such attempts have also been made by using a cellular Potts model (21,22), hybrid discrete-continuum models (8,9), and other computational and mathematical models (3,5,23–25).

This article is organized into three main sections. In the first, we present a new OLHDC model and simulations, and their biological justifications. In the second, we show simulation results from the OLHDC and discuss their significance, and then we conclude, in the third section, with a summary of this work and directions of possible future research.

MODEL AND SIMULATION

The continuum part of the OLHDC model in this article is a system of partial differential equations adopted from the model of Anderson et al. (8,9), with an assumption made that the growth of a generic tumor has just been vascularized, i.e., the formation of blood vessel has occurred. Only three out of the many microenvironmental components affecting tumor growth will be considered in this work: ECM density (denoted by e), MDE concentration (denoted by m), and nutrient concentration (denoted by n). Each of the three variables is dependent on space, $\vec{r}$, and time, t: $e(\vec{r},t)$, $m(\vec{r},t)$, and $n(\vec{r},t)$. Time $t \in [0, t_{\text{last}}]$ and $e(\vec{r},t)$, $m(\vec{r},t)$, and $n(\vec{r},t)$ are computed on a grid of points, $\vec{r} \in \Omega \subset R^{\text{d}}$, where Ω is a bounded domain and d is the dimensionality. Here, for the sake of computational convenience, we consider the case of $d = 2$ although there is no technical reason for not considering $d = 3$. Thus, the results presented here could be interpreted as two-dimensional slices through the center of the three-dimensional tumor cell. However, it is important to note that because cell behavior such as cell migration, cell-cell adhesion, and cell-ECM interaction in three-dimensional environments differs from that in two-dimensional substrates (26–28), it will be required that we modify the OLHDC model accordingly to take into account three-dimensional morphologies and mode of motility when three-dimensional simulations are carried out. In the discrete part of the OLHDC model, cell migration including random and biased movement is described by the Langevin equation (in the form of force balance), incorporated with detailed cell behaviors for cell-cell and cell-ECM interactions, cell proliferation, and cell death. In such a model, if cell motion is determined by internal and external forces, we need to mathematically formulate them first. Unfortunately, there are no exact known macroscopic forces to describe cell-cell (adhesion and repulsion) and cell-ECM interactions (haptotaxis). As a starting point in developing a new off-lattice model, we implemented some reasonable force formulae to describe each interaction based on models for the forces between particles or molecules with repulsive or attractive forms that have been conventionally used in the physics and chemistry literature.

Continuum components of model

Extracellular matrix (ECM)

The ECM includes the interstitial matrix and the basement membranes that are composed of a dense meshwork of collagen, laminin, and heparan sulfate proteoglycans and do not normally contain pores that would allow passive tumor cell migration (1). Due to its diverse composition, the ECM can serve not only as providing support and anchorage for cells, but also as regulating intercellular communication. The ECM is assumed to be degraded by the MDE upon contact as reported in the literature (1,29). The degraded amount of ECM concentration simply depends on the product of ECM and MDE concentrations as

$$\frac{\partial e}{\partial t} = -\alpha m e, \tag{1}$$

where α is the ECM degradation rate by MDE.

Matrix-degrading enzyme (MDE)

The critical role of the MDE is degrading the basement membrane to allow cells to penetrate into the surrounding ECM. However, it also has been known that the MDE can target many non-ECM proteins such as growth factors, growth factor receptors, and cytokines (29). As a consequence, the MDE activity is complex and may act both in favor of tumor promotion and tumor suppression (29). However, in the continuum model of the OLHDC, we assume only the limited role of the MDE, in that the ECM that is degraded by the MDE, which is produced by tumor cells, diffuses into the ECM and undergoes as a certain type of decay. Thus, the MDE concentration is expressed as

$$\frac{\partial m}{\partial t} = D_{\mathrm{m}}\nabla^2 m + \beta c - \gamma m, \tag{2}$$

where D_{m} is the MDE diffusion coefficient, β is the MDE production rate by cells, and γ is the MDE natural decay rate.

Nutrient (oxygen)

Oxygen is a fundamental primary nutrient for tumor cells for survival, growth, and invasion. It is assumed that blood vessel formation, i.e., vascularization, has just been established with continuous oxygen supply through the ECM. In addition, the amount of oxygen supplied by the ECM is simply assumed to be proportional to the ECM density, as was assumed by Anderson et al. (8,9). The oxygen is further assumed to diffuse into the ECM for consumption by tumor cells, and naturally decays. In accordance, the oxygen is described using a diffusion-reaction differential equation as

$$\frac{\partial n}{\partial t} = D_{\mathrm{n}}\nabla^2 n + \delta e - \varphi c - \lambda n, \tag{3}$$

where D_{n}, δ, φ, and λ are the diffusion coefficient, production, consumption, and natural decay rates of the nutrient, respectively.

Discrete component of model

Cell movement (Langevin dynamics)

Cell migration is most commonly and widely described as a persistent random walk motion (30,31) which is emergent from the Langevin equation (32,33),

$$m\frac{d\vec{v}_{\mathrm{i}}(t)}{dt} = -\xi\vec{v}_{\mathrm{i}}(t) + \vec{f}_{\mathrm{i}}^{\,\mathrm{R}}(t), \tag{4}$$

where m is the mass of a single cell, $\vec{v}_{\mathrm{i}}(t)$ is the i^{th} cell velocity, ξ is an effective friction coefficient, and $\vec{f}_{\mathrm{i}}^{\,\mathrm{R}}(t)$ is random force acting on the i^{th} cell. The first term on the right-hand side denotes the friction force accounting for cell-cell and cell-ECM friction, and the second term denotes the random stochastic force. If there are other forces associated with the cell motion, they are added into Eq. 4 as

$$m\frac{d\vec{v}_{\mathrm{i}}(t)}{dt} = -\xi\vec{v}_{\mathrm{i}}(t) + \vec{f}_{\mathrm{i}}^{\,\mathrm{R}}(t) + \vec{f}_{\mathrm{i}}^{\,\mathrm{D}}(t), \tag{5}$$

where $\vec{f}_{\mathrm{i}}^{\,\mathrm{D}}(t)$ values are the deterministic forces acting on the cells that include cell-cell soft sphere repulsion (excluded volume) force (f^{SSR}), cell-cell adhesion force (f^{CCA}), haptotactic force (f^{H}), and other internal cell-related forces that will be described in the following section. The modified Langevin equation (Eq. 5) enables us to incorporate experimentally measurable quantities such as cell speed and the random motility coefficient into our discrete model simulations (see the Supporting Material for details on the use of the Langevin equation to describe cell movement, and simulation length- and timescales). An important advantage of the off-lattice implementation using the Langevin equation is that there is no assumption made about whether the cellular movement is in the diffusive regime ($\langle\Delta r(t)^2\rangle \propto t^1$) or in the ballistic regime ($\langle\Delta r(t)^2\rangle \propto t^2$), or even in the intermediated regime between these.

Cell-cell soft sphere repulsion force (f^{SSR})

A cell has a physical body with which other cells cannot overlap. To simulate this excluded volume of the cell, we use a soft-sphere repulsion (SSR) force, which is derived and modified from a Lennard-Jones potential by differentiating it with respect to the distance between two interacting cells (particles) (34),

$$f^{\mathrm{SSR}}(r) = \begin{cases} \dfrac{48\varepsilon_{\mathrm{SSR}}}{r}\left[\left(\dfrac{\sigma}{r}\right)^{12} - \left(\dfrac{\sigma}{r_{\mathrm{cut}}^{\mathrm{SSR}}}\right)^{12}\right] & \text{if } r \le r_{\mathrm{cut}}^{\mathrm{SSR}} \\ 0 & \text{otherwise} \end{cases}, \tag{6}$$

where σ is the cell diameter, r is the distance between two interacting cells, and $r_{\mathrm{cut}}^{\mathrm{SSR}}$ is a cutoff distance beyond which the interactions are ignored (see Fig. S1 *a*). The $\varepsilon_{\mathrm{SSR}}$ is a SSR parameter that controls the strength of the SSR force and is fixed to be unity, which is large enough to prevent cells from overlapping one another. This SSR force is derived from Lennard-Jones potential, only with short-ranged repulsion (modeled by the r^{-12}). Additional long-ranged attraction

(modeled by the r^{-6}) to account for natural like-like attraction is frequently used to model the interaction between the particles (beads in a bead-spring model of polymers) in coarse-grained representations of macromolecular systems (35); however, we do not include attractive interactions between cells in our model.

Haptotactic force (f^{H})

Cell migration can be driven by various factors such as the directed response to gradients in pressure, chemical substances, and components of the ECM (36). Haptotaxis is the directed motility of cells due to gradients of ECM-bound chemoattractants. In the OLHDC model, we model the haptotactic force, f^{H}, as realistically and simply as possible, such that cells do not respond to infinitely small gradients and cells do not move infinitely fast in large gradient (37). To this end, we use a Michaelis-Menten or Hill function (38) given by

$$f^{H}(\vec{r}) = \varepsilon_{H}\frac{|\nabla e(\vec{r})|^{\eta}}{(\kappa + |\nabla e(\vec{r})|^{\eta})}\frac{\nabla e(\vec{r})}{|\nabla e(\vec{r})|}, \quad (7)$$

where ε_{H} is the haptotactic force coefficient, $\vec{r}$ is the position vector of a cell, and $\nabla e(\vec{r})$ is a gradient of ECM at $\vec{r}$. The value η is the Hill coefficient, which determines how steeply the haptotactic response rises at its threshold value $\nabla e(\vec{r}) = \kappa$ (37). In our simulation, the threshold ECM concentration gradient $\kappa = 0.005$ is selected for allowing a cell to sense it during the small time step $\Delta t = 0.001$ with an ECM degradation rate of $\alpha = 5$. The f^{H} reaches ~90% of its maximum value with the choice of $\eta = 2$ at $\nabla e = 0.21$ (see Fig. S1 *b*). Because cells and ECM mutually affect each other, the ECM rearranges or reorganizes while cells move over the ECM. In the OLHDC, however, this mechanical response of the ECM has not been taken into account in our version of the model; however, in the future, we plan to represent the ECM more explicitly at a coarse-grained molecular level, which will enable mechanical response to be taken into account. When an initial tumor appears in the ECM, tumor cells secrete MDE which then degrades the ECM, resulting in the formation of the gradient of the ECM in a radial direction. Thus, directed motility caused by the haptotactic force is mostly in a radial direction.

In the OLHDC model, cell positions are off-lattice and the motion of the cells and cellular process are coupled with concentration of the microenvironment chemicals. Thus, a cell at any given arbitrary location needs to sample the concentration of microenvironment chemicals. For this purpose, bilinear interpolation method (see the Supporting Material) has been used to calculate chemical concentration ($C(\vec{r})$) and its gradient ($\nabla C(\vec{r})$) at a cell position vector ($\vec{r}$).

Cell-cell adhesion force (f^{CCA}) and other internal cell-related forces

Explicit sticky sites are introduced to model cell-cell adhesion (CCA) as shown in Fig. S2, where the sticky sites locate on the surface of each cell at a distance of the cell radius, $\sigma/2$. CCA force is basically attractive and is modeled using negative cosine force,

$$f^{CCA}(r) = \begin{cases} -\frac{\varepsilon_{CCA}\pi}{2r_{cut}^{CCA}}\cos\left(\frac{\pi r}{2r_{cut}^{CCA}}\right) & \text{if } r \le r_{cut}^{CCA} \\ 0 & \text{otherwise} \end{cases}, \quad (8)$$

where r is the distance between two interacting sticky sites belonging to different cells, and r_{cut}^{CCA} is a cutoff distance beyond which the interactions are ignored (see Fig. S1 *c*). The size of the sticky sites, the range of cell-cell adhesion force f^{CCA}, is determined by cutoff distance r_{cut}^{CCA}. When $r_{cut}^{CCA} = 0.5$, provided the number of sticky sites is three or more, the sticky interaction will be nonzero at all points on the surface of the cell (see Fig. S2). The ε_{CCA} is a CCA parameter that controls its strength. In our model, both ε_{CCA} and the number of sticky sites are used to model CCA strength variation. The CCA force is similar to square-well potential (limiting case of the square-well potential is the sticky-sphere potential (39)), which has been used to study colloidal fluid and successively, to describe the cohesive nature of real, simple liquids (40). Using the cosine force is somewhat arbitrary in our model. However, this soft cosine force is convenient and effective to simulate a nondiverging attractive force on the analogy of using a sine force to simulate excluded volume of monomers in a polymer melt to prevent monomers from overlapping (35,41). Unlike core cells, sticky sites have no excluded volume; therefore, they can overlap as long as core cells do not overlap each other by f^{SSR}.

Sticky sites on the cell surface are connected into their core cell as shown in Fig. S2. To describe this bond, simple harmonic bond force derived from harmonic bond potential is used,

$$f^{HB}(l) = -k_{HB}(l - l_0), \quad (9)$$

where l is the distance between a core cell and its sticky sites, l_0 is an equilibrium bond length, and k_{HB} is the spring constant (which models how strongly cell membrane, including sticky sites, fluctuates, and thus allows us to simulate stiffness of cell membrane). We believe that using harmonic bond force is more realistic than previous models because it reflects the mechanical nature of cell stiffness as well as cell-cell adhesion through sticky site interaction as described earlier, and puts it on a competitive basis with other mechanical forces. The choice of $k_{HB} = 64\ k_{B}T/\sigma^{2}$ leads to cell membrane fluctuation from the equilibrium bond length ($l_0 = 0.5\sigma$ is used, i.e., the bond length is the same as the radius of a cell) being 0.25σ with 95.5% probability, considering that the probability of bond length l would be proportional to the Boltzmann factor of energy state of bond length l,

$$\exp\left(-\frac{k_{HB}(l - l_0)^{2}}{2\ k_{B}T}\right),$$

which forms the normal or Gaussian distribution.

In addition to the spring force, a harmonic angle force derived from harmonic angle potential is introduced for the sticky sites to be distributed properly on the cell surface,

$$f^{\mathrm{HA}}(\theta) = -k_\theta(\theta - \theta_0), \tag{10}$$

where k_θ is the harmonic angle constant. The value θ denotes the angle between the S_1–C and C–S_2 bonds connecting two consecutive bonds S_1–C–S_2, tending to constrain the angle to its equilibrium value θ_0. In our model, the equilibrium angle is $\theta_0 = 2\pi/n_s$, where n_s is the number of sticky sites on a cell. The distribution of sticky sites on a cell surface becomes isotropic at high value of k_θ and random at low k_θ. In our simulation, $k_\theta = 64\ k_BT/rad^2$ is used and angle fluctuation is $<0.25 = 14.3^\circ$ with 95.5% probability as above.

Cell processes

Cell proliferation

Each cell is capable of dividing into two new daughter cells provided the following two conditions are met: 1), the mother cell has reached her proliferation age ($16h(8,9)$ is assumed); and 2), there is enough space for two daughter cells to occupy in the proximity area of the mother cell. In this case, the cell age is the time since the cell was newly divided, and two daughter cells are placed in a way that one replaces the mother cell and the other is spawned at σ from the mother cell. Note that σ is the distance where SSR force becomes zero. This division is assumed to occur immediately and the size of two daughter cells is identical. To decide whether condition 2 is satisfied, local cell density is calculated at a possible random location of the second daughter cell, $r_{\mathrm{cut}}^{\mathrm{SSR}} = \sigma$ from the mother cell. A cell satisfying condition 1 but not condition 2 becomes a quiescent cell, which is assumed to consume nutrient at half the rate of a proliferating cell. Drasdo et al. (16,42) have shown an alternative way to model the cell division process: the mother cell grows until it has doubled its volume and then deforms into two daughter cells.

Cell death and mutation

In our model, necrosis (i.e., cell death, caused by lack of oxygen) takes place when oxygen concentration drops below a critical value. Dead cells (due to the lack of oxygen) take some space which will not be available for other living cells to proliferate in or to move into. It is expected that even if we allow the space of dead cells to be used for other living cells to proliferate in or to move into, those living cells would soon undergo necrosis due to the lack of oxygen.

Tumor cells are assumed to have already undergone p53 mutation, so their genome is in an unstable state and tumor cells are susceptible to higher mutation rates (8). In our model, mutated tumor cells have their unique phenotype that is characterized by proliferation age, oxygen consumption rate, MDE production rate, and the number of sticky sites and cell-ECM interactions. For example, it is assumed that more-aggressive tumor cells have shorter proliferation age, consume more oxygen, produce more MDE, and may or may not have stronger cell-cell interaction (more or less sticky sites) and larger response to gradient of ECM concentration for cell-ECM interaction. Mutation probability is set to be $P_m = 0.1$ and when the mutation occurs, the phenotype of cell is randomly selected.

Two systems of tumor growth and invasion

Two possible scenarios are taken into account. In System A, we consider tumor cells that have a single phenotype with two variations of the haptotactic force coefficient and the number of sticky sites, and do not mutate at all during the simulation run. Thus, the parameter values used in the first scenario are the same as in Table S1. In System B, we study tumor cells that consist of their own different phenotype and that can mutate into other forms of phenotype. In this case, we assume that more aggressive tumor cells have a phenotype of lower proliferation age, higher oxygen consumption rate, higher MDE production rate, more or less cell-cell adhesion, and stronger haptotaxis (increased directed motion). This assumption is made based on experimental observations (1,43–46). We have considered 10 defined phenotypes in our simulation, although we could have chosen more, or fewer, phenotypes without any constraint. Table S2 summarizes a set of parameter values that describe cell behavior in System B.

The brief algorithm of the simulation process is as follows:

Step 1. Initialization of variables.
Step 2. Cell movement.
Step 3. Update of micro-environmental components.
Step 4. Decision on cell death.
Step 5. Cell proliferation.
Step 6. Cell mutation (this step is only applied to the System B).
Step 7. Repetition of Steps 1–6 until the end of the simulation (see the Supporting Material for details of algorithm).

RESULTS AND DISCUSSION

System A: tumor cells with a single phenotype

Fig. 1 depicts snapshots taken at the end of simulations for different values of n_s and ε_H at $\varepsilon_{CCA} = 5$. Red and green cells represent proliferating and quiescent cells, respectively. Overall shape of the tumor is circular; however, some parts of the tumor boundary are irregular and rough. At fixed ε_H value, a greater number of sticky sites lead to smaller tumor size because tumor cells having more sticky sites can attract other cells more strongly by forming a compactly packed structure and providing less space for inner tumor cells to

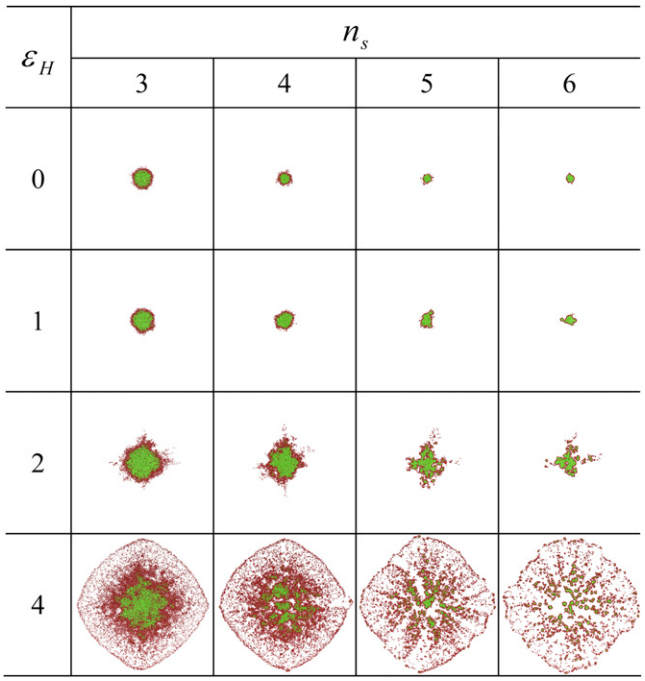

FIGURE 1 Snapshots taken at the end of simulations for different values of n_s and ε_H with $\varepsilon_{CCA} = 5$. Proliferating and quiescent cells are colored in red and in green, respectively.

proliferate. Tumor morphology becomes irregular and forms a fingered shape at $\varepsilon_H = 2$ regardless of n_s value. A further increase in ε_H leads to circular-shaped tumors. In this case, tumors have a less dense outer layer with a denser finger-shaped inner layer at $n_s = 3$ and 4. For $n_s = 5$ and 6, inner dense parts disappear (see Fig. S4 for the evolution of tumor growth at $\varepsilon_H = 4$). It is noted that this less-dense area would be filled with tumor cells if simulations ran longer. Using a mathematical analysis, Castro et al. (4) have showed that: 1), tumor cell proliferation by itself cannot generate the invasive branching behavior; and 2), heterotype chemotaxis gives rise to the onset of tumor invasion.

To describe the dynamics of tumor growth, the number of tumor cells is plotted as a function of time for a system of $n_s = 4$ and ε_{CCA} with various ε_H in Fig. S5. In this figure, the number of proliferating (N_p) and quiescent tumor cells (N_q) are counted separately to investigate whether there are any differences in growth behavior. At first, the total number of tumor cells, N_c, including both proliferating and quiescent cells (plotted in Fig. S5 *a*), is found to change little up to 50 h for almost all the ε_H. After this time, N_c increases gradually for $\varepsilon_H < 1$; dramatically at $\varepsilon_H > 1$; and with intermediate behavior at $\varepsilon_H = 1$. The same trend is also found for N_p in Fig. S5 *b*. N_q shows somewhat different behavior from N_c and N_p in a way that the apparent increase in N_q takes place at a longer time for larger ε_H. In our simulation, we assume that a proliferating cell of an age older than its proliferation age becomes quiescent if there are too many surrounding cells, resulting in no available space for the cell to divide. In other words, the appearance of quiescent cells is an indication of the tumor cells being densely packed. Thus, the earlier appearance of quiescent tumor cells at smaller ε_H is attributed to the denser structure of the tumor initially induced by cell-cell adhesion. Once quiescent tumor cells appear, their ratio to proliferating tumor cells grows almost linearly (see Fig. S5 *d*).

As another dynamic property of tumor growth, we analyze tumor size in terms of radius of gyration of a tumor,

$$R_g = \left(N_c^{-1} \sum_{i=1}^{N_c} (\vec{r}_i - \vec{r}_{cm})^2 \right)^{1/2},$$

where N_c is the total number of tumor cells and $\vec{r}_i$ values are the distances of tumor cells from the center-of-mass of the tumor ($\vec{r}_{cm}$). Bru et al. (3) have grown in vitro two-dimensional tumor monolayers from C6 rat astrocyte glioma and observed a linear growth of the tumor diameter with time. This behavior was also found from a single-cell-based model (47) of tumor growth with a Langevin-type cell motility. In our simulation, we observed that tumor size as a function of time is of a scale-variant behavior and is strongly affected by haptotactic response to ECM gradient, as shown in Fig. 2 *a*. In this figure, $n_s = 4$ and $\varepsilon_{CCA} = 5$ are used as in Fig. S5. It is noted that the general trend of tumor growth as a function of time does not change much for all other values of n_s. At $\varepsilon_H = 0$, the exponent, q, of tumor growth on time, $R_g \propto t^q$, monotonically increases and seems to approach unity. At $\varepsilon_H = 1$, q is 0.5 and this exponent value does not change much within our simulation time. Other than these two cases, there is more than one transition in q value. An initial q value is larger for higher ε_H value, whereas after the first transition, the q value becomes close to 0.5 regardless of ε_H value. If there is another transition like at $\varepsilon_H = 2$, the q value seems to approach unity after the second transition as in the case of $\varepsilon_H = 0$. Interestingly, the first transition is found to take place when quiescent tumor cells begin to appear.

We note that the linear growth ($R_g \propto t^1$) of tumor size is observed when the growth takes place mostly at the border of the tumor (3): Let us assume that the number of tumor cells is proportional to the circular tumor area, $\pi(R/\sigma)^2$, where R is the tumor radius and σ is the cell diameter. Given such a condition, the growth rate is proportional to the number of tumor cell on the circumference of the tumor, $2\pi(R/\sigma)$. When equated with this, we have

$$d\left(\pi(R/\sigma)^2\right)/dt = k \cdot 2\pi(R/\sigma),$$

i.e., $R = R_0 + k\sigma t$, where k is a proportional coefficient and R_0 is the tumor radius at $t = 0$.

Fig. 2 *b* illustrates how the tumor size is related to the total number of tumor cells. If tumor shape is circular in two dimensions and the tumor cells are compactly packed, the total number of tumor cells is proportional to the circular

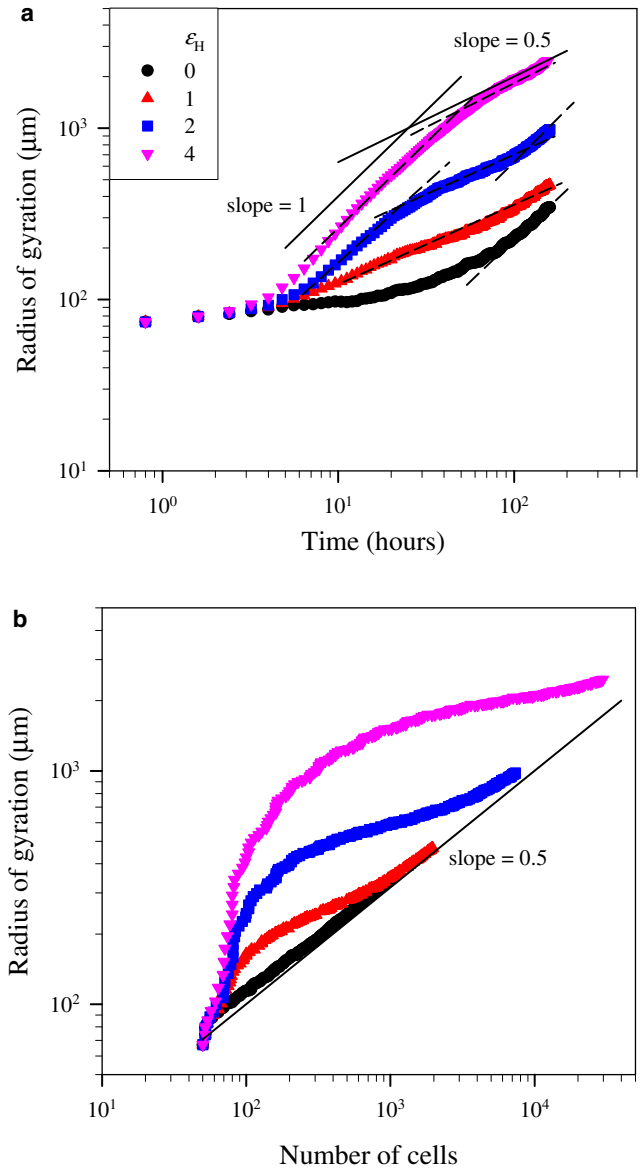

FIGURE 2 Plots showing the radius of gyration of tumor (*a*) as a function of time and (*b*) number of tumor cells, N_c. The system parameters used in this figure are the same in Fig. S5. The solid lines represent the slope being equal to 0.5 and 1. Note that the dashed lines drawn through the symbols are guides to the eye.

area of tumor: $\pi(R/\sigma)^2 \propto N_c$. Thus, this relation leads to $R \propto N_c^{1/2}$. Note that if the same simulation had been carried out in three dimensions, $R \propto N_c^{1/3}$ would be expected because N_c is proportional to tumor volume, $4\pi/3(R/\sigma)^3$. (More generally, $R \propto N_c^{1/d}$, where d is the dimensionality.) As expected, the exponent value asymptotically approaches 0.5 in the end of simulations, indicating a densely packed tumor shape. Interestingly, at $\varepsilon_H \geq 2$, there is a regime where the tumor size does not change much despite the increase in N_c, which indicates that tumor morphology undergoes a dramatic change. At this high value of haptotactic coefficient ($\varepsilon_H \geq 2$), because of the strong haptotactic response to ECM gradient, directed motility of tumor cells in the radial direction causes early tumor morphology to be finger–shaped, with little solid tumor core. Hence, as a tumor grows, the inner tumor region is filled with proliferating cells resulting in little change in the tumor size, while retaining the branch shape to some degree.

Tumor morphology analysis may provide a means of predicting its malignant nature because the morphological asymmetry of tumors has been used as one of the indicators of malignancy (19,20). In this regard, tumor morphology is quantified in terms of tumor roughness defined as

$$R_{\text{rough}} = \frac{1}{N_{\text{bin}}} \sum_{i=1}^{N_{\text{bin}}} \left((d_i - \langle d \rangle)^2 \right)^{1/2}, \tag{11}$$

where N_{bin} is the number of fan-shaped bins made along the circumference of a circle with a bin angle; $2\pi/N_{\text{bin}}$, d_i is a distance of a tumor cell farthest from the tumor center in the i^{th} bin; and $\langle d \rangle$ is the average of d_i, i.e.,

$$\langle d \rangle = N_{\text{bin}}^{-1} \sum_{i=1}^{N_{\text{bin}}} d_i$$

(in our simulation, $N_{\text{bin}} = 36$). Fig. 3 shows time evolution of tumor roughness at various ε_H with $n_s = 4$ and $\varepsilon_{CCA} = 5$. In the case of $\varepsilon_H < 2$, tumor roughness increases in a short time and gradually becomes saturated; however, one or two cases at each fixed value of n_s exhibit a continuous increase within our simulation time (see tumor morphology shown in Fig. 1.) This continuous increase in tumor roughness implies strong tumor invasiveness mainly due to haptotaxis that may overcome cell-cell adhesion. Bru et al. (3) reported a superrough dynamics on the growth of C6 rat astrocyte glioma which

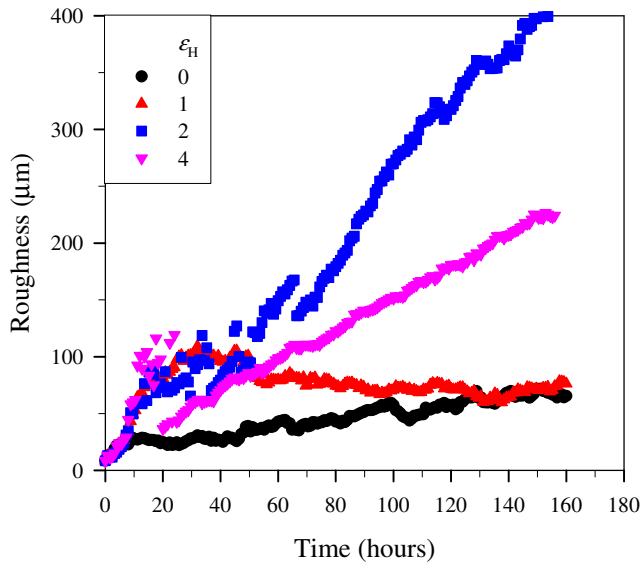

FIGURE 3 Time evolution of tumor roughness at $n_s = 4$ and $\varepsilon_{CCA} = 5$ with various values of ε_H. All other parameter values are the same as in Table S1.

exhibits $w \propto L^{\eta}$ with $\eta > 1$, where w, L, and η are width (in our case, R_{rough}), contour length of circular tumor interface, and roughness exponent, respectively. From our simulation, we also made a plot of tumor roughness versus its size, particularly for finger-shape tumors; however, no superrough behavior has been observed (data not shown).

System B: mixture of tumor cells with various phenotypes

System B1 uses parameter values that are dependent on tumor cell phenotype (described in Table S2) with a fixed number of sticky sites. In doing so, we can study an important role of cell-cell adhesion affecting tumor morphology. First of all, it is expected that smaller n_s and lower ε_{CCA} leads to a larger tumor, as observed in Fig. 1; this behavior is also seen in Fig. 4. However, the tumor size little depends on n_s at $\varepsilon_{CCA} = 0$ because sticky sites with no interaction among them do nothing for cell-cell adhesion. More-aggressive tumor cells divide more frequently due to their shorter proliferation age. Thus, there are more-aggressive tumor cells that consume more oxygen and secrete more MDE that can degrade ECM. Because oxygen is assumed to be produced by the ECM, if there is degradation of the ECM, oxygen concentration decreases more quickly. When there is lack of oxygen, tumor cells undergo apoptosis. This oxygen-deficient region usually appears in the center of the tumor, because of limitation of oxygen diffusion into this area. In our simulation, dead tumor cells, colored in black, are also observed in the center of tumor, as seen in Fig. 4. When $n_s \geq 4$ and $\varepsilon_{CCA} = 5$, or $n_s = 3$ and $\varepsilon_{CCA} = 10$, initial tumor growth is asymmetric (see Fig. S6), because more-aggressive tumor cells escaping from an initial tumor colony are nonuniformly distributed. Despite this initial asymmetric tumor growth, final tumor shape is circular, as seen for the systems of $n_s \geq 4$ with $\varepsilon_{CCA} = 5$. When $n_s \geq 4$ and $\varepsilon_{CCA} = 10$, a tumor does not grow much, because of the significant increase in cell-cell adhesion. This observation leads to possible strategies for prevention and intervention of tumor metastasis by boosting the strength of cell-cell adhesion.

System B2 is subdivided into two cases, Systems B2-1 and B2-2, based on the dependence of the number of sticky sites, n_s on tumor cell phenotype: More-aggressive tumor cells may have either fewer sticky sites (lower n_s) in System B2-1 or a greater number of sticky sites (higher n_s) in System B2-2. These two conflicting circumstances have been experimentally observed. For example, E-cadherin (cell-cell adhesion molecules) mediated cell-cell adhesion prevents invasiveness of human carcinoma cells (46). In addition, it has been naturally believed that aggressive tumor cells must lose their adhesion to other cells to escape from tumor aggregation. However, it has also been observed that more-invasive tumor cells exhibit evidence of stronger cell-cell adhesion (48).

Fig. 5 shows snapshots taken at the end of simulations for Systems B2-1 and B2-2. Tumor cells in System B2-1 form a circular-shaped tumor with dead cells in the central region, which is similar to the one found in Fig. 4. Although initial

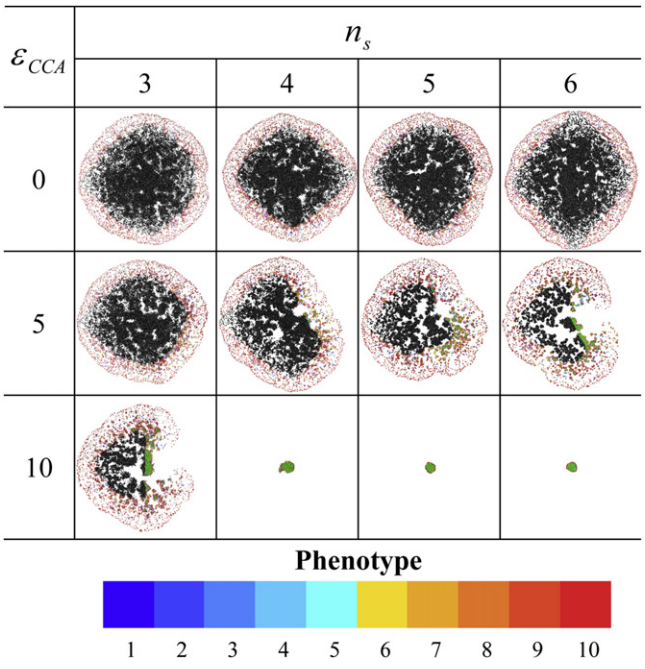

FIGURE 4 Snapshots taken at the end of simulations for a mixture of tumor cells with various phenotypes at fixed values of n_s and ε_{CCA}. Other parameter values used in this figure are the same as in the Table S2. Color bars represent tumor cell phenotype, and quiescent and dead cells are colored green and black, respectively.

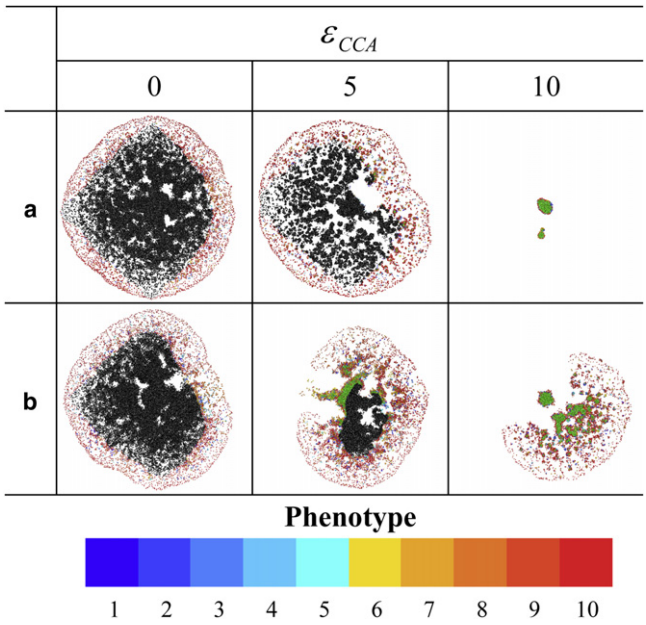

FIGURE 5 Snapshots taken at the end of simulations for a mixture of tumor cells with phenotype-dependent n_s. More-aggressive tumor cells have (*a*) less or (*b*) more n_s. The color code used in this figure is the same as in Fig. 4.

asymmetric tumor growth is observed in both Systems B2-1 and B2-2, System B2-2 shows longer asymmetric tumor growth at $\varepsilon_{CCA} = 5$. Interesting tumor morphology is found at $\varepsilon_{CCA} = 10$ for System B2-1. In this case, tumor cells with $n_s = 5$ or $n_s = 6$ and higher ε_H escape from the original tumor colony, proliferate, and form another tumor colony. These two tumor colonies are merged-into-one in longer simulation (see Fig. S7). In general, tumor morphologies are thought to depend on competing processes between cell proliferation destabilizing the tumor surface and cell-cell adhesion stabilizing this surface (22,23). Our simulations suggest that haptotaxis also plays a role in determining tumor morphology in the early stage of tumor growth: i.e., cells could escape from the original tumor colony, proliferate, and form another tumor colony when the cells have strong haptotactic response. To our knowledge, this is the first model to observe that tumor cells escape from the original tumor colony by haptotaxis to form another tumor colony.

CONCLUSIONS

There are two aims in this work. One is to develop a hybrid model of tumor growth and invasion with, compared to previous models, more realistic descriptions of cell-cell adhesion, cell-ECM interaction, and cell migration using the Langevin equation. The other is to study the effect of cell-cell adhesion and haptotaxis on tumor growth and its morphological behavior by performing systematic simulations of the OLHDC model. We have developed an OLHDC model of tumor growth and invasion, combining the continuum description of micro-environment variables and the discrete description of cellular behavior, including cell motility and cell cycle. A phenomenologically realistic and bio/physically relevant model describing for cell motility is developed using the well-known framework of a persistent random walk with the Langevin equation. Cell-cell adhesion and cell-ECM interaction play an important role in tumor growth and morphological change. In our model, cell-cell adhesion is described by explicit sticky sites, and cell-ECM interaction through haptotactic force is modeled using a Hill function. In our model, we assume that sticky sites bound to cell surface fluctuate within 25% of cell diameter from the cell surface. We can tune more- or less-fluctuating cell membrane, including sticky sites, to simulate soft or stiff cells, respectively. Considering that the cell stiffness of metastatic cancer cells is >70% softer than the benign cells (49), one of the advantages in using our OLHDC model is that we can address the effect of stiffness of cancer cells on tumor growth and invasion in future work.

It is demonstrated that the tumor growth and its morphology are strongly affected by cell-cell adhesion and haptotaxis by means of the number of proliferating and quiescent tumor cells, radius of gyration of tumors, and their roughness. In the case of tumor cells with a single phenotype, if the effect of n_s and ε_{CCA} is stronger than that of ε_H, a small circular tumor develops. When the effect of ε_H is comparable to that of n_s and ε_{CCA}, tumor morphology becomes finger-shaped, with high tumor roughness. If the effect of ε_H is stronger than that of n_s and ε_{CCA}, overall tumor shape becomes circular with less dense outer layer and denser inner finger-shape. In our simulation, tumor cells are compactly packed. The relation between the size of tumor and the number of tumor cells is of a power-law form, $R \sim N_c^{1/d}$, and we found the exponent value asymptotically approaches 0.5 in the end of simulations regardless of n_s and ε_H.

Tumor cells with various phenotypes initially develop asymmetric tumor morphology because more-aggressive cells escaping from an initial tumor colony are nonuniformly distributed; however, they eventually form a circular shape. It is noted that although the OLHDC adopts continuum models from the model of Anderson et al. (8,9) there are some tumor morphologies that the Anderson model cannot predict but are observed in our Fig. S4, where small tumor colonies form inner part of the tumor, and in Fig. S7, where certain tumor cells escape from the original tumor colony, form a new tumor colony, and merge into the original one. We speculate that these different morphologies are mainly due to explicit force treatment for cell-cell interaction via sticky sites and cell-ECM interaction through a haptotactic force of the Hill function form, because these morphologies were not observed when the haptotactic force was simply assumed to be linearly proportional to ECM gradient.

One limit of the OLHDC model is that, by using an off-lattice model, whereas the direction and displacement in cell motion are not restricted at all, they can be affected when cell motion is coupled with a haptotactic force that calculated on a lattice: i.e., the haptotactic force is a function of gradient of ECM concentration calculated at any given arbitrary location of a cell using bilinear interpolation method with four nearest-neighbor lattice grid points. Thus, the OLHDC model cannot completely overcome lattice anisotropy. To surmount this obstacle, a triangular lattice instead of a square lattice may be desirable (50,51). In lattice gas simulations, for example, Navier-Stokes transport processes are only represented realistically on high-connectivity lattices but, in two dimensions, the triangular lattice has the minimum required connectivity (six nearest neighbors per lattice point versus four for a square lattice). Ultimately, we will develop a purely off-lattice description for all microenvironment variables to avoid any lattice anisotropy.

SUPPORTING MATERIAL

Seven figures and two tables are available at http://www.biophysj.org/biophysj/supplemental/S0006-3495(09)01573-2.

This work is supported by the National Cancer Institute under grant No. 5U54CA113007-04.

REFERENCES

1. Stetler-Stevenson, W. G., S. Aznavoorian, and L. A. Liotta. 1993. Tumor cell interactions with the extracellular matrix during invasion and metastasis. *Annu. Rev. Cell Biol.* 9:541–573.
2. Anderson, A. R. A., and V. Quaranta. 2008. Integrative mathematical oncology. *Nat. Rev. Cancer.* 8:227–234.
3. Bru, A., J. M. Pastor, …, C. Berenguer. 1998. Super-rough dynamics on tumor growth. *Phys. Rev. Lett.* 81:4008–4011.
4. Castro, M., C. Molina-París, and T. S. Deisboeck. 2005. Tumor growth instability and the onset of invasion. *Phys. Rev. E Stat. Nonlin. Soft Matter Phys.* 72:041907.
5. Khain, E., and L. M. Sander. 2006. Dynamics and pattern formation in invasive tumor growth. *Phys. Rev. Lett.* 96:188103.
6. Schaller, G., and M. Meyer-Hermann. 2006. Continuum versus discrete model: a comparison for multicellular tumor spheroids. *Philos. Trans. Roy. Soc. A Math. Phys. Eng. Sci.* 364:1443–1464.
7. Drasdo, D., R. Kree, and J. S. McCaskill. 1995. Monte Carlo approach to tissue-cell populations. *Phys. Rev. E Stat. Phys. Plasmas Fluids Relat. Interdiscip. Topics.* 52:6635–6657.
8. Anderson, A. R. A. 2005. A hybrid mathematical model of solid tumor invasion: the importance of cell adhesion. *Math. Med. Biol.* 22:163–186.
9. Anderson, A. R. A., A. M. Weaver, …, V. Quaranta. 2006. Tumor morphology and phenotypic evolution driven by selective pressure from the microenvironment. *Cell.* 127:905–915.
10. dos Reis, A. N., J. C. M. Mombach, …, L. F. de Avila. 2003. The interplay between cell adhesion and environment rigidity in the morphology of tumors. *Physica A.* 322:546–554.
11. Ferreira, S. C., Jr., M. L. Martins, and M. J. Vilela. 2002. Reaction-diffusion model for the growth of avascular tumor. *Phys. Rev. E Stat. Nonlin. Soft Matter Phys.* 65:021907.
12. Gerlee, P., and A. R. A. Anderson. 2007. An evolutionary hybrid cellular automaton model of solid tumor growth. *J. Theor. Biol.* 246:583–603.
13. Jiang, Y., J. Pjesivac-Grbovic, …, J. P. Freyer. 2005. A multiscale model for avascular tumor growth. *Biophys. J.* 89:3884–3894.
14. Kim, Y., M. A. Stolarska, and H. G. Othmer. 2007. A hybrid model for tumor spheroid growth in vitro. I. Theoretical development and early results. *Math. Models Meth. Appl. Sci.* 17:1773–1798.
15. Ramis-Conde, I., M. A. J. Chaplain, and A. R. A. Anderson. 2008. Mathematical modeling of cancer cell invasion of tissue. *Math. Comput. Model.* 47:533–545.
16. Drasdo, D., and S. Höhme. 2005. A single-cell-based model of tumor growth in vitro: monolayers and spheroids. *Phys. Biol.* 2:133–147.
17. Potdar, A. A., J. Lu, …, P. T. Cummings. 2009. Bimodal analysis of mammary epithelial cell migration in two dimensions. *Ann. Biomed. Eng.* 37:230–245.
18. Codling, E. A., M. J. Plank, and S. Benhamou. 2008. Random walk models in biology. *J. R. Soc. Interface.* 5:813–834.
19. Rangayyan, R. M., N. R. Mudigonda, and J. E. L. Desautels. 2000. Boundary modeling and shape analysis methods for classification of mammographic masses. *Med. Biol. Eng. Comput.* 38:487–496.
20. Landini, G., and J. W. Rippin. 1996. How important is tumor shape? Quantification of the epithelial-connective tissue interface in oral lesions using local connected fractal dimension analysis. *J. Pathol.* 179: 210–217.
21. Knewitz, M. A., and J. C. M. Mombach. 2006. Computer simulation of the influence of cellular adhesion on the morphology of the interface between tissues of proliferating and quiescent cells. *Comput. Biol. Med.* 36:59–69.
22. Popławski, N. J., U. Agero, …, A. R. Anderson. 2009. Front instabilities and invasiveness of simulated avascular tumors. *Bull. Math. Biol.* 71:1189–1227.
23. Frieboes, H. B., X. Zheng, …, V. Cristini. 2006. An integrated computational/experimental model of tumor invasion. *Cancer Res.* 66:1597–1604.
24. Cristini, V., H. B. Frieboes, …, J. Sinek. 2005. Morphologic instability and cancer invasion. *Clin. Cancer Res.* 11:6772–6779.
25. Sanga, S., H. B. Frieboes, …, V. Cristini. 2007. Predictive oncology: a review of multidisciplinary, multiscale in silico modeling linking phenotype, morphology and growth. *Neuroimage.* 37 (Suppl 1): S120–S134.
26. Weaver, V. M., O. W. Petersen, …, M. J. Bissell. 1997. Reversion of the malignant phenotype of human breast cells in three-dimensional culture and in vivo by integrin blocking antibodies. *J. Cell Biol.* 137:231–245.
27. Cukierman, E., R. Pankov, …, K. M. Yamada. 2001. Taking cell-matrix adhesions to the third dimension. *Science.* 294:1708–1712.
28. Friedl, P., and E. B. Bröcker. 2000. The biology of cell locomotion within three-dimensional extracellular matrix. *Cell. Mol. Life Sci.* 57:41–64.
29. DeClerck, Y. A., A. M. Mercurio, …, M. Padarathsingh. 2004. Proteases, extracellular matrix, and cancer: a workshop of the path B study section. *Am. J. Pathol.* 164:1131–1139.
30. Selmeczi, D., S. Mosler, …, H. Flyvbjerg. 2005. Cell motility as persistent random motion: theories from experiments. *Biophys. J.* 89: 912–931.
31. Kipper, M. J., H. K. Kleinman, and F. W. Wang. 2007. New method for modeling connective-tissue cell migration: improved accuracy on motility parameters. *Biophys. J.* 93:1797–1808.
32. Saltzman, W. M. 2004. Tissue Engineering: Engineering Principles for the Design of Replacement Organs and Tissues. Oxford University Press, New York.
33. Doi, M., and S. F. Edwards. 1986. The Theory of Polymer Dynamics. Oxford University Press, New York.
34. Frenkel, D., and B. Smit. 2001. Understanding Molecular Simulation: From Algorithms to Applications. Academic Press, New York.
35. Binder, K., editor. 1995. Monte Carlo and Molecular Dynamics Simulations in Polymer Science. Oxford University Press, New York.
36. Mallet, D. G., and G. J. Pettet. 2006. A mathematical model of integrin-mediated haptotactic cell migration. *Bull. Math. Biol.* 68:231–253.
37. Glazier, J. A., A. Balter, and N. J. Poplawski. 2007. Magnetization to morphogenesis: a brief history of the Glazier-Graner-Hogeweg Model. *In* Single-Cell Based Models in Biology and Medicine. A. R. A. Anderson, M. A. J. Chaplain, and K. A. Rejniak, editors. Birkhauser, Boston, MA.
38. Michaelis, L., and M. Menten. 1913. Die Kinetik der Invertinwirkung. *Biochem. Z.* 49:333–369.
39. Baxter, R. J. 1968. Percus-Yevick equation for hard spheres with surface adhesion. *J. Chem. Phys.* 49:2770–2774.
40. Bergenholtz, J., and N. J. Wagner. 1994. The Huggins coefficient for the square-well colloidal fluid. *Ind. Eng. Chem. Res.* 33:2391–2397.
41. Auhl, R., R. Everaers, …, S. J. Plimpton. 2003. Equilibration of long chain polymer melts in computer simulations. *J. Chem. Phys.* 119:12718–12728.
42. Drasdo, D., S. Hoehme, and M. Block. 2007. On the role of physics in the growth and pattern formation of multi-cellular systems: what can we learn from individual-cell based models? *J. Stat. Phys.* 128: 287–345.
43. Böhle, A. S., and H. Kalthoff. 1999. Molecular mechanisms of tumor metastasis and angiogenesis. *Langenbecks Arch. Surg.* 384:133–140.
44. Takeichi, M. 1993. Cadherins in cancer: implications for invasion and metastasis. *Curr. Opin. Cell Biol.* 5:806–811.
45. Kim, D., S. Kim, …, J. Chung. 2001. Akt/PKB promotes cancer cell invasion via increased motility and metalloproteinase production. *FASEB J.* 15:1953–1962.
46. Frixen, U. H., J. Behrens, …, W. Birchmeier. 1991. E-cadherin-mediated cell-cell adhesion prevents invasiveness of human carcinoma cells. *J. Cell Biol.* 113:173–185.

47. Drasdo, D. 2007. Center-based single-cell models: an approach to multi-cellular organization based on a conceptual analogy to colloidal particles. *In* Single-Cell Based Models in Biology and Medicine. A. R. A. Anderson, M. A. J. Chaplain, and K. A. Rejniak, editors. Birkhauser, Basel, Switzerland.

48. Anderson, A. R. A., M. Hassanein, …, A. M. Weaver. 2009. Microenvironmental independence associated with tumor progression. *Cancer Res*. 66:8797–8806.

49. Cross, S. E., Y. S. Jin, …, J. K. Gimzewski. 2007. Nanomechanical analysis of cells from cancer patients. *Nat. Nanotechnol*. 2: 780–783.

50. Frisch, U., B. Hasslacher, and Y. Pomeau. 1986. Lattice-gas automata for the Navier-Stokes equation. *Phys. Rev. Lett*. 56, 1505–150.

51. Dhumieres, D., P. Lallemand, and U. Frisch. 1986. Lattice gas models for 3D hydrodynamics. *Europhys. Lett*. 2:291–297.